RSC Advances

PAPER

View Article Online
View Journal | View Issue

Check for updates

Cite this: *RSC Adv.*, 2020, **10**, 8936

A high performance surface acoustic wave visible light sensor using novel materials: Bi_2S_3 nanobelts

Chong Li,†[a] Hao Kan,†[ab] Jingting Luo, *[a] Chen Fu,*[a] Jian Zhou,[c] Xueli Liu,[d] Wen Wang,[d] Qiuping Wei [e] and Yongqing Fu [f]

Received 28th October 2019
Accepted 10th December 2019

DOI: 10.1039/c9ra08848b

rsc.li/rsc-advances

Low dimensional Bi_2S_3 materials are excellent for use in photodetectors with excellent stability and fast response time. In this work, we developed a visible light sensor with good performance based on surface acoustic wave (SAW) devices using Bi_2S_3 nanobelts as the sensing materials. The SAW delay-line sensor was fabricated on ST-cut quartz with a designed wavelength of 15.8 microns using conventional photolithography techniques. The measured center frequency was 200.02 MHz. The Bi_2S_3 nanobelts prepared by a facile hydrothermal process were deposited onto SAW sensors by spin-coating. Under irradiation of 625 nm visible light with a power intensity of 170 μW cm^{-2}, the sensor showed a fast and large response with a frequency upshift of 7 kHz within 1 s. The upshift of the frequency of the SAW device is mainly attributed to the mass loading effect caused by the desorption of oxygen from the Bi_2S_3 nanobelts under visible light radiation.

Open Access Article. Published on 02 March 2020. Downloaded on 5/23/2026 4:53:37 AM.
This article is licensed under a Creative Commons Attribution-NonCommercial 3.0 Unported Licence.

Introduction

Over the past few decades, Surface Acoustic Wave (SAW) devices have been widely used in industrial fields for components such as radio frequency filters and oscillators.[1] They can be effectively produced by fabricating interdigital transducers (IDTs) on the surface of piezoelectric substrates.[2] SAW devices have the advantages of good stability, low power consumption and wireless transmission, *etc*, and they are also very sensitive to any external stimulation or changes on the surface. Therefore, SAW devices have great potential to be used as biosensors, gas sensors, pressure sensors, photodetectors and so on.[3–8]

In recent years, photodetectors based on SAW devices have received extensive attention.[9–11] For example, Pang *et al.* fabricated a $LiTaO_3$-based Love mode SAW ultraviolet (UV) sensor with ZnO top layer,[12] which was operated at a resonant frequency of 41.5 MHz, with a frequency shift of 150 kHz under 254 nm UV radiation at 350 μW cm^{-2} Zhou *et al.* used MoS_2 nanosheets as the UV-sensitive layer for SAW photodetectors,[8] which showed a maximum frequency shift of 3.5 MHz under a 365 nm UV illumination at a power density of 1.466 mW cm^{-2}. However, there are few reports about visible-light sensors or infrared sensors based on the SAW devices. These photodetectors can be extensively used in electronic eyes,[13] tumor detection,[14] and imaging.[15]

Bismuth sulfide (Bi_2S_3) is one of the important group V and VI binary chalcogenide semiconductors with a narrow band-gap of 1.3 eV, good environmental stability and large absorption coefficient. It has been widely used in solar cells, photocatalytic and so on.[16–18] Furthermore, it has an orthorhombic structure which has an inherent anisotropic crystal structure along the [001] direction, thus making it possible for the preferential growth into 1D nanostructure.[19] For example, Yu *et al.* synthesized uniform Bi_2S_3 nanorods with tuneable lengths, which exhibited excellent responses to visible light.[20] Li *et al.* prepared Bi_2S_3 hollow sphere nanostructures using a hydrothermal method.[21] The photoconductivity of the photodetector made using these hollow spheres demonstrated excellent stability and fast response time towards visible light. Konstantatos prepared solution-processed photoconductive detector based on Bi_2S_3 nanocrystals, which showed good responsivity (40 A W^{-1}) under visible light radiation.[22] However, there are no reports about SAW photodetectors based on Bi_2S_3 nanomaterials. It is critical to develop such a high performance photodetector based on SAW resonator using Bi_2S_3 nanomaterials, which will have advantages of wireless control, battery-less operation and high sensitivity because of the merits from SAW devices.

In this work, we demonstrated, for the first time, a high performance surface acoustic wave visible light photodetector

[a]*Shenzhen Key Laboratory of Advanced Thin Films and Applications, College of Physics and Optoelectronic Engineering, Shenzhen University, 518060, Shenzhen, China. E-mail: luojt@szu.edu.cn; chenfu@szu.edu.cn*

[b]*Key Laboratory of Optoelectronic Devices and Systems of Ministry of Education and Guangdong Province, College of Optoelectronic Engineering, Shenzhen University, 518060, Shenzhen, China*

[c]*State Key Laboratory of Advanced Design and Manufacturing for Vehicle Body, College of Mechanical and Vehicle Engineering, Hunan University, Changsha 410082, China*

[d]*Institute of Acoustics, Chinese Academy of Sciences, 100190, Beijing, China*

[e]*School of Materials Science and Engineering, State Key Laboratory of Powder Metallurgy, Central South University, Changsha 410083, China*

[f]*Faculty of Engineering and Environment, Northumbria University, Newcastle upon Tyne, NE1 8ST, UK*

† These authors have equal contribution.

This journal is © The Royal Society of Chemistry 2020

Open Access Article. Published on 02 March 2020. Downloaded on 5/23/2026 4:53:37 AM.
This article is licensed under a Creative Commons Attribution-NonCommercial 3.0 Unported Licence.

using novel materials: Bi_2S_3 nanobelts. In our strategy, Bi_2S_3 nanobelts were synthesized using a hydrothermal method and then spin-coated onto a ST-cut quartz SAW device. The SAW device had very good response to the visible light and the sensing mechanisms were discussed.

Experimental section

Material synthesis

Bi_2S_3 nanobelts were prepared using a hydrothermal method reported in the literature.[23] Briefly, triphenyl bismuth ($C_{18}H_{15}Bi$, 98%, Aladdin, 0.6 mM) and dibenzyl disulfide ($C_6H_5CH_2$-$SSCH_2C_6H_5$, 98%, Aladdin, 0.6 mM) were dissolved in 4 ml oleylamine (OLA), and then 0.4 g polyvinyl pyrrolidone (PVP, Aladdin, MW ≈ 24 000–28 000) were dissolved into 26 ml absolute ethanol. After that, these solutions were thoroughly mixed together and transferred into a 50 ml autoclave to react at 180 °C for 8 hours. Finally, the product was washed with hexane and dissolved in ethanol at a concentration of 30 mg ml^{-1} for use.

Sensor fabrication and measurements

Quartz is a widely used piezoelectric material, which has a low temperature coefficient, low sound velocity and very good stability. In this study, a ST-cut quartz is chosen as the piezoelectric substrate for making the SAW delay-line device. A schematic diagram is shown in Fig. 1a. The input IDTs consist of 220 finger pairs and the output IDTs have 95 finger pairs. The sensitive area of the SAW device is 3.6 mm^2. All the aluminium based IDTs were fabricated through a conventional photolithography technique. The measured center frequency was 200.02 MHz. The obtained optical microscope image of the device is shown in Fig. 1b.

For the sensitive layer deposition, 50 μL of Bi_2S_3 nanobelts solution was spin-coated (at a speed of 1500 rpm) onto the sensitive area of the SAW resonator as a photosensitive material. The central frequency of SAW delay-line device was measured using a network analyzer (Keysight, E5071C). A 625 nm light-emitting diode was precisely controlled through a functional generator (JDS6600) for acting as a light source. The intensity of the incident light was measured using a power meter (Thermo Fisher Scientific). A schematic illustration of the testing system was shown in Fig. 2.

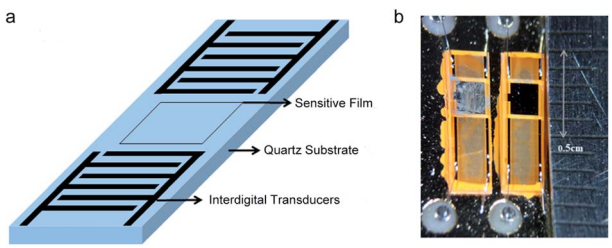

Fig. 1 (a) A schematic illustration, and (b) an optical microscope image of the ST-cut quartz SAW device.

Microstructures of the sensing material were studied using a field emission scanning electron microscopy (FE-SEM, Supra 55 Sapphire) and a high-resolution transmission electron microscopy (HR-TEM, JEOL-2100). Crystallization of the Bi_2S_3 nanobelts were characterized using the X-ray diffraction (XRD, Ultima IV) with CuKα radiation that was operated at 30 kV and 30 mA. The UV-Vis absorption spectrum was measured using a UV/Vis/NIR spectrometer (PerkinElmer Lambda 950).

Results and discussion

Microstructure and morphology of the samples

A low-magnification and a high-magnification SEM image are shown in Fig. 3a and b, respectively, which revealed 1-D belt-shaped structure of as-synthesized Bi_2S_3. The average length of the synthesized nanobelts is about five to twenty micrometres and the width is about fifty to three hundred nanometres. A uniform and porous layer formed on the sensitive area of the quartz substrate. TEM image provides detailed information about the morphology and the structural features of the as-synthesized Bi_2S_3 nanobelts, *e.g.*, a 1-D strip-like nanostructure shown in Fig. 3c. The HR-TEM image in Fig. 3d clearly shows the lattice spacing of 0.353 nm, which corresponds to the (310) planes of orthorhombic Bi_2S_3 phase.

Fig. 4a shows a typical XRD pattern of the Bi_2S_3 nanobelts. Clearly, all the diffraction peaks are consistent with the orthorhombic structure of bulk Bi_2S_3 (JCPDS card no. 17-0320). These is no extra diffraction peaks from other materials, which indicates that high-purity Bi_2S_3 nanomaterials were synthesized. Fig. 4b demonstrates the UV-Vis absorption spectrum of the Bi_2S_3 nanobelts, which have an obvious and broad optical absorption peak from 300–700 nm, implying their potentials for applications in UV-Vis photodetectors.

Visible light sensing performance

Fig. 5 shows the transmission signals (S_{12}) of resonant frequencies of SAW delay-line device with and without Bi_2S_3 nanobelts sensing layer. The central frequency of the SAW device as fabricated is 200.02 MHz and the insertion loss is −12.82 dB. After coating Bi_2S_3 nanobelts film, the central frequency decreased and the insertion loss increased as the

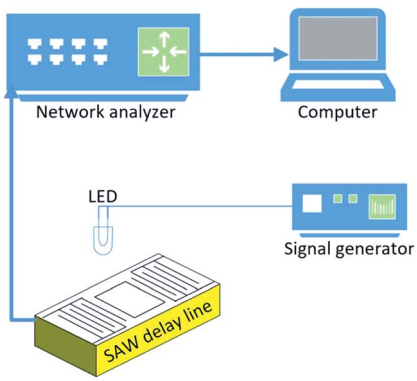

Fig. 2 Schematic illustration of the experimental setup.

Open Access Article. Published on 02 March 2020. Downloaded on 5/23/2026 4:53:37 AM.
This article is licensed under a Creative Commons Attribution-NonCommercial 3.0 Unported Licence.

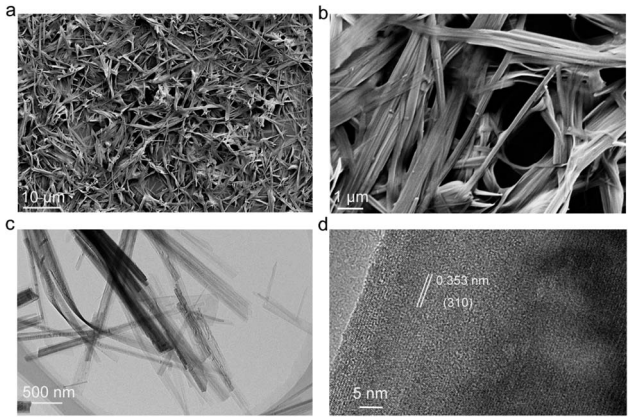

Fig. 3 SEM image of the Bi_2S_3 nanobelts film (a) at low magnification (b) at high magnification. (c) TEM image and (d) HR-TEM image of the Bi_2S_3 nanobelts.

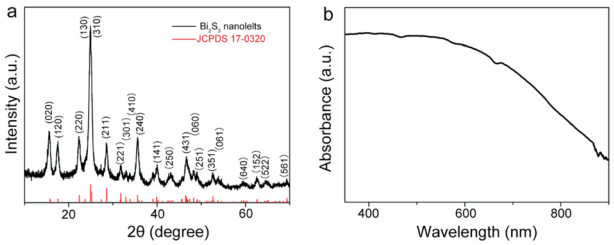

Fig. 4 (a) XRD pattern of the prepared Bi_2S_3 nanobelts. (b) UV-visible absorption spectrum of Bi_2S_3 nanobelts.

result of the mass loading effect and the wave diffraction due to the addition of Bi_2S_3 nanobelts film.

Fig. 6a shows frequency evolution curves of the SAW visible light sensor under different light intensities with a wavelength of 625 nm. Clearly, the sensor exhibits a positive frequency shift when the light switch on and the working frequency of the SAW device recover to its initial value when the light switch off. Upon three repeated on/off cycles using the LED, the dynamic response curves for three cycles are almost identical with each other under the same light intensity. This result indicates that

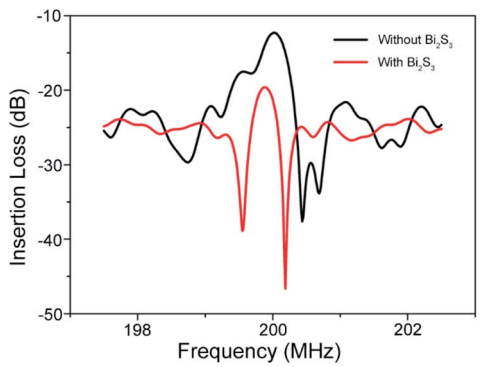

Fig. 5 Measured transmission signals (S_{12}) of resonant frequencies for the SAW device with and without Bi_2S_3 nanobelts.

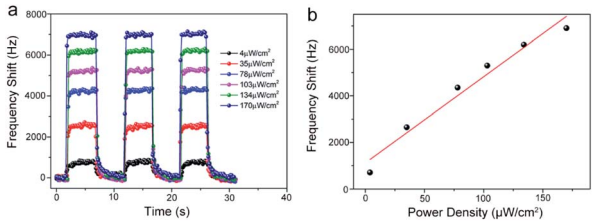

Fig. 6 (a) Photo responses of the SAW photodetector based on Bi_2S_3 nanobelts under 625 nm visible light with different power densities. (b) The dependence of frequency shift on power intensities under 625 nm visible light.

the SAW visible light sensor using Bi_2S_3 nanobelts has good repeatability and reproducibility. In addition, the frequency shifts of the sensor are increased with the increase of visible light power density. The frequency-shifts as large as 7 kHz when the light intensity increased to 170 μW cm^{-2}. The curve of the frequency-shifts dependence on light intensity was plotted in Fig. 6b. The frequency-shifts are enhanced with increasing light intensity and will not show any saturation due to the low density of the incident light. The frequency-shift of the device is 300 Hz, even under the illumination with an optical power as low as 4 μW cm^{-2}.

The sensitivities (S) is the most important parameter for SAW photodetector, it can be calculated from the following equation.

$$S = \frac{\Delta f / f}{P} \quad (1)$$

where Δf is frequency-shifts, f is resonant frequency of device, P is the power density of incident light. From eqn (1), we can calculate the sensitivity of the SAW visible light sensor based on Bi_2S_3 nanobelts for 625 nm light source and the obtained sensitivity is 0.2 ppm (μW cm^{-2})$^{-1}$. For comparison, Table 1 summarizes the photodetector based on SAW. This SAW photodetector exhibits relatively high sensitivity under visible light illumination.

The central frequency shift of the SAW light sensor can be ascribe to the acousto-electric interaction effect, mass-loading effect and the elastic effect.[24] Generally, under visible light radiation, the photo-generated carries will decrease the SAW velocity due to acoustoelectric effect,[25] and hence the SAW central frequency will downshift. However, the central frequency is upshift under visible light radiation in our experiment. Therefore, the acoustoelectric effect can't be the dominated reason for this work. It should be noted in our work that the ST-cut quartz substrate have a low electro-mechanical coupling coefficient, *e.g.*, $k^2 = 0.11\%$.[26] Therefore, the acousto-electric effect may have a low effect on our SAW device.

On the other hand, the mass-loading effect result in a change in frequency shift (Δf) is given by:[27]

$$\Delta f = -c_m f_0^2 \Delta m_s \quad (2)$$

where C_m is the coefficient of mass sensitivity, Δm_s is the mass loading change.

This journal is © The Royal Society of Chemistry 2020

Open Access Article. Published on 02 March 2020. Downloaded on 5/23/2026 4:53:37 AM.
This article is licensed under a Creative Commons Attribution-NonCommercial 3.0 Unported Licence.

Table 1 Sensitivity comparison of SAW based photodetectors

Materials	Piezoelectric substrate	Central frequency	Wavelength	Sensitivity (ppm $(\mu W\ cm^{-2})^{-1}$)	Ref.
ZnO film	$LiNbO_3$	36.3 MHz	365 nm	0.12	28
ZnO nanoparticles	YZ $LiNbO_3$	64 MHz	345 nm	2.8	29
ZnO nanowire	128° YX $LiNbO_3$	50.9 MHz	365 nm	8.765	30
ZnO nanoparticles	128° YX $LiNbO_3$	235 MHz	365 nm	3.34	31
MoS_2 nanosheets	ZnO	1.02 GHz	365 nm	2.05	8
Bi_2S_3 nanobelts	ST-cut quartz	200.02 MHz	625 nm	0.2	This work

In this work, we suggest the photo response of Bi_2S_3 nanobelts related to the oxygen adsorption and desorption on Bi_2S_3 nanomaterials. Fig. 7 shows a schematic illustration of adsorption and desorption of oxygen on Bi_2S_3 nanobelts coated on IDT/quartz structure under dark and visible light radiation. Under a dark condition, oxygen molecules could capture free electrons from the nanobelts through the following equation.

$$O_2 + e^- \rightarrow O_2^- \quad (3)$$

Upon illumination by visible light, there will be electron–hole pairs generated in the nanobelts. The adsorbed oxygen molecules on Bi_2S_3 nanobelts will capture the photo-generated holes, which discharged *via* a reaction as below.

$$O_2^- + h^+ \rightarrow O_2 \quad (4)$$

Thereby the mass loading of the film reduced under light irradiation due to the oxygen discharge, which promotes the acoustic wave propagation and thus increase the central frequency. In this work, the Bi_2S_3 nanobelts films with lots of porous have contributed to the adsorption and desorption of oxygen molecules (Fig. 3a and b). Therefore, with increasing incident light intensity from 4 to 170 $\mu W\ cm^{-2}$, more excited photo-carriers are produced by higher light intensity, thus more oxygen ions will be released. Therefore, the frequency shift will be larger. After the light switched off, oxygen ions will be re-absorbed again. Hence, the mass loading increased due to the oxygen re-absorption, which goes against the acoustic wave propagation and thus the centre frequency returns back.

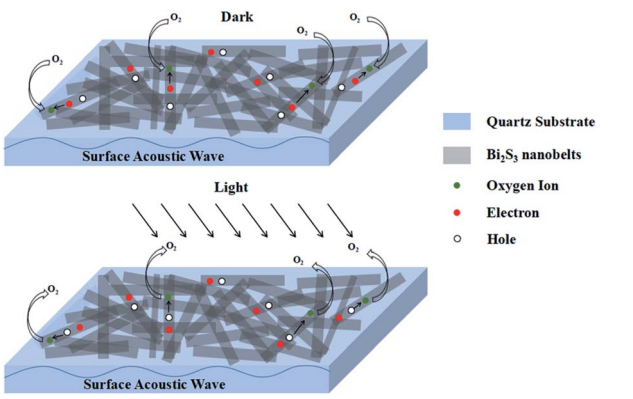

Fig. 7 Schematic illustration of sensing mechanisms of adsorption and desorption of oxygen on Bi_2S_3 nanobelts.

Conclusions

In this work, we demonstrate a high performance SAW visible light sensor using novel materials, Bi_2S_3 nanobelts, for the first time. The frequency upshifts of the SAW photodetector reached as high as 7 kHz upon 625 nm with intensity of 170 $\mu W\ cm^{-2}$. Further, the SAW visible light sensor exhibited a sensitivity of about 0.2 ppm $(\mu W\ cm^{-2})^{-1}$ and a good linear characteristic within the range from 4 to 170 $\mu W\ cm^{-2}$. Due to a low electro-mechanical coupling coefficient of ST-cut quartz SAW devices, the upshift of frequency of the SAW photodetector might not be ascribed to the acoustoelectric effect. On the other hand, the mass loading effect pay the main role in the upshift of frequency of the SAW photodetector caused by the desorption of oxygen from the Bi_2S_3 nanobelts under visible light radiation. This facile fabrication of a fast and large response SAW visible light sensor using Bi_2S_3 nanobelts offers a novel method for visible light photodetector devices in practical applications.

Conflicts of interest

There are no conflicts to declare.

Acknowledgements

The authors gratefully acknowledge the support of the National Key Research and Development Program of China (grant no. 2016YFB0402705), State Key Laboratory of Powder Metallurgy, Central South University, the China Postdoctoral Science Foundation (2019M653018). This work was also supported by National Natural Science Foundation of China (grant no. 11704261, 51605485, 11575118), Shenzhen Science & Technology Project (grant no. JCYJ20170817100658231, JCYJ20180507182439574, JCYJ20180305124317872). Funding supports from UK Engineering Physics and Science Research Council (EPSRC EP/P018998/1).

References

1 A. Pohl, *IEEE Trans. Ultrason. Ferroelectrics Freq. Contr.*, 2000, **47**, 317–331.

Open Access Article. Published on 02 March 2020. Downloaded on 5/23/2026 4:53:37 AM.
This article is licensed under a Creative Commons Attribution-NonCommercial 3.0 Unported Licence.

2 R. M. White and F. W. Voltmer, *Appl. Phys. Lett.*, 1965, **7**, 314–316.
3 M. Goran, M. Tina, K. Wöllner and G. Gauglitz, *Surf. Coat. Technol.*, 2006, **201**, 1282–1288.
4 Y. Q. Fu, J. K. Luo, N. T. Nguyen, A. J. Walton, A. J. Flewitt, X. T Zu, Y. Li, G. McHale, A. Matthews, E. Iborra, H. Du and W. I. Milne, *Prog. Mater. Sci.*, 2017, **89**, 31–91.
5 Y. Liu, H. Huang, L. L. Wang, D. P. Cai, B. Liu, D. D. Wang, Q. H. Li and T. H. Wang, Electrospun CeO_2 nanoparticles/PVP nanofibers based high-frequency surface acoustic wave humidity sensor, *Sens. Actuators, B*, 2016, **223**, 730–737.
6 L. Rana, R. Gupta, R. Kshetrimayumb, M. Tomarc and V. Guptaa, *Surf. Coat. Technol.*, 2018, **343**, 89–92.
7 S. Liu, G. Xu, Z. Ni, X. Guo, L. Luo, J. Tu and D. Zhang, *Appl. Phys. Lett.*, 2017, **111**, 043508.
8 P. Zhou, C. Chen, X. Wang, B. Hu and H. San, *Sens. Actuators, A*, 2018, **271**, 389–397.
9 C. Fu, K. Lee, K. Lee and S. Yang, *Smart Mater. Struct.*, 2015, **24**, 01501.
10 M. Thepnurat, P. Ruankham, S. Phadunghitidhada, A. Gardchareon, D. Wongratanaphisan and S. Choopun, *Surf. Coat. Technol.*, 2016, **306**, 25–29.
11 W. Peng, Y. He, Y. Xu, S. Jin, K. Ma, X. Zhao, X. Kang and C. Wen, *Sens. Actuators, A*, 2013, **199**, 149–155.
12 H. Pang, Y. Fu, Z. Li, Y. Li, J. Ma, F. Placido, A. J. Walton and X. Zu, *Sens. Actuators, A*, 2013, **193**, 87–94.
13 H. Ko, M. P. Stoykovich, J. Song, V. Malyarchuk, W. M. Choi, C. Yu, J. B. Geddes, J. Xiao, S. Wang, Y. Huang and J. A. Rogers, *Nature*, 2008, **454**, 748–753.
14 X. Gao, Y. Cui, R. M. Levenson, L. W. K. Chung and S. Nie, *Nat. Biotechnol.*, 2004, **22**, 969–976.
15 H. Kan, W. Zheng, R. Lin, M. Li, C. Fu, H. Sun, M. Dong, C. Xu, J. Luo, Y. Fu and F. Huang, *ACS Appl. Mater. Interfaces*, 2019, **11**, 8412–8418.
16 A. K. Rath, M. Bernechea, L. Martinez and G. Konstantatos, *Adv. Mater.*, 2011, **23**, 3712–3717.
17 G. Li, X. Chen and G. Gao, *Nanoscale*, 2014, **6**, 3283–3288.
18 S. Vadivel, A. N. Naveen, V. P. Kamalakannan, P. Cao and N. Balasubramanian, *Appl. Surf. Sci.*, 2015, **351**, 635–645.
19 M. B. Sigman and B. A. Korgel, *Chem. Mater.*, 2005, **17**, 1655–1660.
20 H. Yu, J. Wang, T. Wang, H. Yu, J. Yang, G. Liu, G. Qiao, Q. Yang and X. Cheng, *CrystEngComm*, 2017, **19**, 727–733.
21 H. Li, J. Yang, J. Zhang and M. Zhou, *RSC Adv.*, 2012, **2**, 6258–6261.
22 G. Konstantatos, L. Levina, J. Tang and E. H. Sargent, *Nano Lett.*, 2008, **8**, 4002–4006.
23 H. Kan, M. Li, Z. Song, S. Liu, B. Zhang, J. Liu, M. Li, G. Zhang, S. Jiang and H. Liu, *J. Colloid Interface Sci.*, 2017, **506**, 102–110.
24 J. D. Gailpeau, R. S. Falconer, J. F. Vetelino, J. J. Caron, E. L. Wittman, M. G. Schweyer and J. C. Andle, *Sens. Actuators, B*, 1995, **24**, 49–53.
25 A. J. Ricco, S. J. Martin and T. E. Zipperian, *Sens. Actuators, B*, 1985, **8**, 319–333.
26 L. Rana, R. Gupta, M. Tomar and V. Gupta, *Sens. Actuators, B*, 2017, **252**, 840–845.
27 J. D. N. Cheeke and Z. Wang, *Sens. Actuators, B*, 1999, **59**, 146–153.
28 P. Sharma and K. Sreenivas, *Appl. Phys. Lett.*, 2003, **83**, 3617.
29 V. Chivukula, D. Ciplys, M. Shur and P. Dutta, *Appl. Phys. Lett.*, 2010, **96**, 233512.
30 W. Peng, Y. He, C. Wen and K. Ma, *Sens. Actuators, A*, 2012, **184**, 34–40.
31 K. J. Lee, H. Oh, M. Jo, K. Lee and S. Yang, *Microelectron. Eng.*, 2013, **111**, 105–109.

This journal is © The Royal Society of Chemistry 2020